Journal of Structural Geology 32 (2010) 960–974

Contents lists available at ScienceDirect

Journal of Structural Geology

journal homepage: www.elsevier.com/locate/jsg

Buckling folds of a single layer embedded in matrix – Folding behavior revealed by numerical analysis

Kuo-Pin Huang [a], Kuo-Jen Chang [b], Tai-Tien Wang [c], Fu-Shu Jeng [a,*]

[a] Department of Civil Engineering, National Taiwan University, Taipei, Taiwan
[b] Department of Civil Engineering, National Taipei University of Technology, Taipei, Taiwan
[c] Department of Materials and Mineral Resources Engineering, National Taipei University of Technology, Taipei, Taiwan

ARTICLE INFO

Article history:
Received 10 September 2008
Received in revised form
6 May 2010
Accepted 4 June 2010
Available online 11 June 2010

Keywords:
Buckling fold
Numerical analysis
Elastic
Viscous
Post-buckle
Strain rate

ABSTRACT

Theoretical solutions have been proposed recently for various competent layer–matrix systems, including elastic, viscous and elasto-viscous materials. Furthermore, three type fold-forms of buckling fold had been proposed. These solutions were obtained based on the most simplified, one-dimensional governing equations. Therefore, these solutions require further validation by observing the two-dimensional folding behaviors. This work utilizes numerical analyses to study the buckling and post-buckling behaviors of various layer–matrix systems. As a result, it was found that for competence contrast $R \geqq 10$ the fold-forms obtained by numerical simulation agree well with those theoretical solutions. Three types of fold-forms can be generated and the resulting wavelengths are also close to the predictions. The fold evolution during the post-buckling stage is explored up to high amplitudes, and the results indicate that the fold-forms can remain the same or be changed from one type to another type, depending on the types of layer–matrix system, the applied strain rates, the original fold-forms at buckling, etc. The fold behaviors from buckling to the post-buckling stage of the layer–matrix systems are presented.

1. Introduction

For a stiff, competent layer of rock stratum embedded in relatively softer matrix, the lateral compression of this competent layer–matrix system can induce folding of the rock stratum and surrounding matrix, which is often referred as buckle-folding. Research on buckle-folding can be dated to the early 1900s (Smoluchowski, 1909). Field observations and interpretations focused on formation, wavelength and thickness have been made regarding the appearance of folds and mechanism (Sherwin and Chapple, 1968; Donath and Parker, 1964; Hudleston, 1986; Hudleston and Lan, 1993). To further explore the mechanism, studies based on laboratorial experiments to explore evolution have been conducted (Biot et al., 1961; Hudleston, 1973b; Fletcher, 1974; Dubey and Cobbold, 1977; Abbassi and Mancktelow, 1990, 1992; Mancktelow and Abbassi, 1992; Treagus and Sokoutis, 1992). Theoretical solutions considering various material types (elastic, viscoelastic and viscous) have accordingly been developed (Karman and Biot, 1940; Biot, 1957, 1959, 1961; Currie et al., 1962; Ramberg, 1961, 1963, 1964; Chapple, 1968; Smith, 1975, 1977, 1979; Jeng et al., 2001; Jeng and Huang, 2008), and the fold formation in deformed layers are considered according to the competence contrast between layer and matrix. Studies considered in more sophisticated conditions have also been conducted, e.g. for single layer systems (Chapple, 1969; Cobbold, 1975, 1976, 1977; Fletcher, 1974, 1977; Hudleston, 1973a,b; Hudleston and Stephansson, 1973; Hudleston and Lan, 1994; Hunt et al., 1996a,b; Kocher et al., 2008; Lan and Hudleston, 1991, 1996; Mancktelow, 1999; Mühlhaus et al., 1994; Schmalholz and Podladchikov, 1999, 2000; Treagus, 1973; Williams et al., 1977; Zhang et al., 1996, 2000); for stress–strain analysis (Dieterich and Carter, 1969; Hobbs, 1971; Hudleston et al., 1996; Treagus, 1981, 1983, 1999, 2003); for bending folds (Latham, 1985a,b); for deformation rate (Price, 1975; Johnson and Fletcher, 1994; Mühlhaus et al., 1998, 2002a,b; Schmalholz and Podladchikov, 2001a,b,c; Treagus, 2003); for heterogeneous deformation (Passchier et al., 2005); for nonperiodic folds (Whiting and Hunt, 1997) and a brief summary is given by Price and Cosgrove (1990). In these studies, folding with a single wavelength, the so-called dominant wavelength, has been recognized.

In addition to the findings of previous researches, folds with dual wavelength or decaying amplitude were found possible, when considering the solutions in a more general manner (Mühlhaus et al., 1998; Jeng et al., 2001, 2002; Jeng and Huang, 2008; Hobbs

* Corresponding author. Department of Civil Engineering, National Taiwan University, No. 1, Sec. 4, Roosevelt Rd, Taipei 10617, Taiwan. Tel./fax: +886 2 2364 5734.
E-mail address: fsjeng@ntu.edu.tw (F.-S. Jeng).

0191-8141/$ – see front matter © 2010 Elsevier Ltd. All rights reserved.
doi:10.1016/j.jsg.2010.06.002

Table 1
$\varepsilon_x^B - l$ relationships of three fold-forms, expressed in terms of R_E and R_V, for various models (Jeng and Huang, 2008).

	Material layer–matrix	Fold-form*		
		Type A	*Type B* (l_d)	*Type C*
1.	*E–E*	$\varepsilon_x^B = (\pi^2/3l^2) + (l/2R_E\pi)$	$l_d = 2\pi\sqrt[3]{R_E/6}$	$\varepsilon_x^B = (2\pi^2/l^2) - \sqrt{3\pi/4R_El}$
2.	*V–V*	$\varepsilon_x^B = (\pi^2/3l^2) + (l/2R_V\pi)$	$l_d = 2\pi\sqrt[3]{R_V/6}$	$\varepsilon_x^B = (2\pi^2/l^2) - \sqrt{3\pi/4R_Vl}$
3.	*EV–EV*	$\varepsilon_x^B = (\pi^2/3l^2) + (l(1-e^{-T/T_{R0}}))/(2R_V\pi(1-e^{-(R_E/R_V)(T/T_{R0})}))$	$l_d = 2\pi\sqrt[3]{R_V/6}[(1-e^{-(R_E/R_V)(T/T_{R0})})/(1-e^{-(T/T_{R0})})]^{1/3}$	$\varepsilon_x^B = (2\pi^2/l^2) - \sqrt{(3\pi/4R_Vl)((1-e^{-(T/T_{R0})})/(1-e^{-(R_E/R_V)(T/T_R)}))}$
4.	*E–EV*	$\varepsilon_x^B = \pi^2/3l^2 + (l/\overline{R}_E(T/T_{R0})\pi)(1-e^{-(T/T_{R0})})$	$l_d = 2\pi\sqrt[3]{\overline{R}_E(T/T_{R0})/12}[1/(1-e^{-(T/T_{R0})})]^{1/3}$	$\varepsilon_x^B = 2\pi^2/l^2 - \sqrt{3\pi(1-e^{-(T/T_{R0})})/2\overline{R}_El(T/T_{R0})}$
5.	*EV–V*	$\varepsilon_x^B = \pi^2/3l^2 + (l/2R_V\pi(1-e^{-(T/T_R)}))$	$l_d = 2\pi\sqrt[3]{R_V/6}[1-e^{-(T/T_R)}]^{1/3}$	$\varepsilon_x^B = 2\pi^2/l^2 - \sqrt{3\pi/4R_Vl(1-e^{-(T/T_R)})}$
6.	*E–V*	$\varepsilon_x^B = \pi^2/3l^2 + (l/\pi(T/(T_R)_{E-V}))$	$l_d = 2\pi\sqrt[3]{(1/12)(T/(T_R)_{E-V})}$	$\varepsilon_x^B = 2\pi^2/l^2 - \sqrt{3\pi/2l(T/(T_R)_{E-V})}$

*Remarks:
1. $R_E = \overline{E}/E_o = \overline{G}/G_o$; $\overline{R}_E = \overline{G}/G_o$; $R_V = \eta/\eta_o$; $T_R = \eta/G$; $T_{R0} = \eta_o/G_o$; $(T_R)_{E-V} = \eta_o/\overline{G}$.
2. The symbols and their definitions please refer to Jeng and Huang (2008).

et al., 2008). Furthermore, it is necessary to consider that the material properties of the competent layer and the matrix may change with the local environments e.g. temperature and pressure conditions. These conditions can be simply expressed in elastic, viscoelastic and viscous materials. The three types of material can have six kinds of possible combinations for real geological conditions. Two-component notations are used hereafter to indicate the layer–matrix system. For instance, the notations *E–E*, *E–EV*, *E–V* represent the cases of an elastic layer respectively embedded in the elastic, viscoelastic and viscous matrix. The solutions for six possible models (*E–E*, *E–EV*, *E–V*, *EV–EV*, *EV–V* and *V–V*) have been established (Biot, 1961; Currie et al., 1962; Jeng and Huang, 2008).

It was identified that the resulting waveforms depend on the amount of compression, and could be expressed in terms of lateral force or lateral strain in rock layer, when bucking (or folding) occurs. The relation of the lateral compression at the moment of buckling (ε_x^B) and the resulting wavelength l for the six aforementioned models is conveniently summarized in Table 1 (Biot, 1961; Currie et al., 1962; Jeng and Huang, 2008). In general, the $\varepsilon_x^B - l$ relationship has the typical appearance as shown in the left-side of Fig. 1. The upper curve is related to the fold-form with dual-frequencies and the lower curve is the fold-form with single frequency yet with decaying amplitude. The intersection of the upper and the lower curves is the *Type B* fold-form, which is also referred as fold-form at critical state (Biot, 1961; Currie et al., 1962). These three types of fold-form are depicted in the right-side of Fig. 1. Among these six models, *E–E* and *V–V* models are found to be strain rate-independent and the other four models are strain rate-dependent (Jeng and Huang, 2008). For convenience, Table 2 summarizes the response of the six models when subjected to extreme strain rates.

In developing theoretical solutions for the six models, two-dimensional folding phenomena are simplified as one-dimensional governing equations (Biot, 1961; Currie et al., 1962; Hunt et al., 1996a,b; Schmalholz and Podladchikov, 1999, 2000; Jeng and Huang, 2008). Therefore, there is still a suspicion that the one-dimensional governing equations yielding solutions may not be adequate to simulate two-dimensional buckling fold-forms. Moreover, the governing equation is the state of force (or stress) equilibrium at the moment of buckling and thus the solutions can only represent the fold-form at the moment of buckling. The folding evolution throughout entire deformation history after the buckling stage is important. Thus, it is of interest to ask what will happen after the buckling? Can the fold-form maintain same wavelength? Or, will the wavelength, even the type of fold-form, be changed after the folds have been generated, during the post-buckling stage of deformation? For the sake of convenience, the deforming process after the fold initiation is called post-buckling stage.

Previous research indicated that numerical simulations based on finite element method yielded reasonable fold-forms. The resulting dominant fold-form by numerical simulation with high competence contrast agreed with the theoretical solution (Zhang et al., 1996, 2000; Mancktelow, 1999, 2001; Jeng et al., 2002). As to other models (*E–EV*, *EV–EV*, *EV–V*, *E–V*), comparisons are not completely made because some solutions have been only recently proposed (Jeng and Huang, 2008). This research aimed at exploring the above-mentioned questions based on two-dimensional numerical analyses. The observations focus on: What are the types of fold-form corresponding to different degrees of lateral compression? This also means: can three types of fold-form really happen in numerical simulation? How well do the resulting wavelengths agree with the theoretical solutions as summarized in Table 1? Are these models really rate-dependent or rate-independent as described by the theoretical solutions? What is the

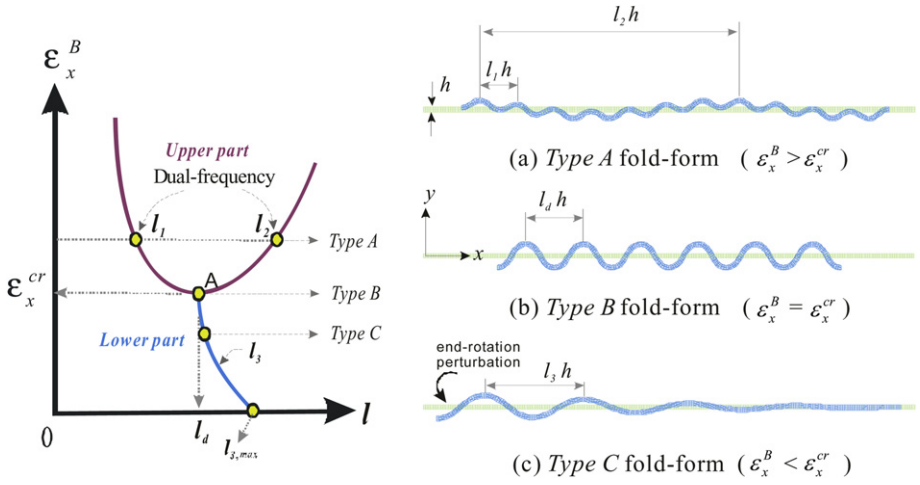

Fig. 1. Schematic illustration of the three types of fold-forms and the $\varepsilon_x^B - l$ relationships, which have been obtained from analytical solutions (Jeng and Huang, 2008). (a) *Type A* fold-form comprises two frequencies, which can be yielded when $\varepsilon_x^B > \varepsilon_x^{cr}$. (b) *Type B* fold-form is a single frequency-wave with a constant amplitude over the full length of the competent layer (when $\varepsilon^B = \varepsilon_x^{cr}$). (c) *Type C* fold-form is a single frequency-wave characterized by an amplitude attenuation away from the perturbed end (when $\varepsilon^B < \varepsilon_x^{cr}$).

structural evolution of the fold? Will the fold-form change in the post-buckling stage? Lastly, the folding behavior of lower competence contrast ($R \leq 50$) will be explored.

2. Setup of numerical analysis

This work uses a finite element code, ABAQUS, to simulate the fold-forms for the six possible models, and the results are compared to the theoretical solutions listed in Table 1.

2.1. Material models

For a pure elastic material, the conventional isotropic, linear elastic model is selected. The constitutive relation for such material is defined as:

$$\sigma_{ij} = \lambda\varepsilon_{kk}\delta_{ij} + G\varepsilon_{ij} \tag{1}$$

where: σ_{ij} is stress tensor; ε_{ij} is strain tensor; ε_{kk} is volume strain; δ_{ij} is the Kronecker delta; λ and G ($=\mu$) are Lamé constants; G is shear modulus or modulus of rigidity. For isotropic, elastic material, λ can be expressed in terms of E and ν as $\lambda = \nu/((1+\nu)(1-2\nu))$ $E = (2\nu/1-2\nu)G$, where E and ν are Young's modulus and Poisson's ratio. If the Poisson's ratios assigned for the layer and the matrix are different, they can affect folding behavior of the layer–matrix system. On the other hand, it can be shown that if they are the same, then Poisson's ratio will not affect folding behavior. For the sake of convenience, as in previous research, the influence of Poisson's ratio is excluded by setting both the layer and the matrix to have same Poisson's ratio of 0.5.

Table 2
Conversion of the layer–matrix system to other material models upon extreme strain rates (Jeng and Huang, 2008).

	Original type of material (layer–matrix)	Converted material type		Remarks
		Very fast strain rate	Very slow strain rate	
1	*E–E*	*E–E*	*E–E*	Strain rate-independent
2	*V–V*	*V–V*	*V–V*	
3	*EV–EV*	*E–E*	*V–V*	Strain rate-dependent
4	*E–EV*	*E–E*	*E–V* (no matrix)	
5	*EV–V*	–	*V–V*	
6	*E–V*	–	No matrix	

For pure viscous material, the stress is related to the strain rate of viscous flow as:

$$\sigma_{ij} = \left(p - \frac{2}{3}\eta\dot{\varepsilon}_{kk}\right)\delta_{ij} + 2\eta\dot{\varepsilon}_{ij} \tag{2}$$

where η is viscosity; p ($=\sigma_{ii}/3$) is hydrostatic stress; $\dot{\varepsilon}_{kk}$ is volume strain rate and $\dot{\varepsilon}_{ij}$ is strain rate tensor. When the viscous material is incompressible, so that there will be no volume strain rate ($\dot{\varepsilon}_{kk} = 0$), Eq. (2) can be reduced to $\sigma_{ij} = p\delta_{ij} + 2\eta\dot{\varepsilon}_{ij}$, which is called Newtonian flow.

For the elasto-viscous material, a Maxwell model is adopted, and the stress is comprised of rate-independent elastic component and rate-dependent viscous component as:

$$\dot{\varepsilon}_{ij} = \frac{\sigma_{ij}}{2\eta} + \frac{\dot{\sigma}_{ij}}{2G} \tag{3}$$

In order to compare the results of numerical analyses of this work with other published works, all the elastic, viscous and elasto-viscous models are set to be incompressible for convenience. As a result, Eq. (3) can be reduced to $\dot{\varepsilon}_{ij} = (\sigma'_{ij}/2\eta) + (\dot{\sigma}'_{ij}/2G)$, where $\sigma'_{ij}(= \sigma_{ij} - p\delta_{ij})$ is deviatoric stress tensor.

For geologically realistic conditions, based on the composition of quartz–feldspar, the viscosity ratio seldom exceeds 20 (Hobbs et al., 2008). However, there are several rock material compositions which may give large values of competence contrast, ranging from 50 to 100, e.g. metapsammite and calcsilicate layers versus the embedding marbles (Druguet et al., 2009). On the other hand, Schmalholz and Podladchikov (2001a) proposed a method to estimate strain and competence contrast from fold shape and verified it by analogue and numerical experiment. The results show the competence contrast ranges from 10 to 250. Overall, a compromise ratio from 50 to 100 between the low and high competence contrast can be usually used for fold analysis and numerical modeling (Treagus and Fletcher, 2009).

The input parameters for the three types of materials (elastic, viscous and elasto-viscous) are summarized in Table 3. The competence contrast assigned for elastic layer–matrix system is $R_E = 100$, which was often adopted in previous researches, so that all the results can be compared on a similar basis. As to viscous material, the competence contrast is set to be $R_V = 1000$, since R_V is often much greater than R_E in reality, and which value is also adopted in many previous researches.

Table 3
Material properties used by numerical analyses.

Material model	Layer			Matrix		
	λ (Pa)	μ (Pa)	η (Pa s)	λ_o (Pa)	μ_o (Pa)	η_o (Pa s)
Elastic	1×10^{15}	1×10^{12}		1×10^{13}	1×10^{10}	
Viscoelastic	1×10^{15}	1×10^{12}	1×10^{20}	1×10^{13}	1×10^{10}	1×10^{17}
Viscous			1×10^{20}			1×10^{17}

Remarks:
1. Herein, with and without the subscript "o" represent the properties of competent layer and matrix, respectively.
2. λ, μ and λ_o, $\mu_o$are Lamé constant of competent layer and matrix, respectively. η and η_o are viscosity.
3. For isotropic elastic material, $\lambda = (2\nu/1-2\nu)G$, where ν is Poisson's ratio. Similarly, $\mu = G$, where G is shear modulus.
4. In this table, competence ratios for elastic and viscous materials are respectively set to be: $R_E = \mu/\mu_o(=\lambda/\lambda_o) = 100$; $R_V = (\eta/\eta_o) = 1000$.

2.2. Numerical models

The geometry of the model and boundary constraints are similar to those adopted by previous research (Zhang et al., 1996, 2000; Mancktelow, 1999; Jeng et al., 2002), so as to allow direct comparisons. The competent layer has a length of 210 h, where h is the thickness of the layer, as depicted in Fig. 2. The matrix has a thickness of 70 h on both sides of the layer and a "roller" constraint (free slip in horizontal direction and no vertical displacement) is imposed along the right and the lower boundaries of the model.

If a perfectly straight layer without any perturbation is compressed, the layer is shortened without buckling. A perturbation is therefore required to induce folding in a numerical analysis and some initial geometric configurations different from a perfect-straight layer were generally adopted for this purpose (Zhang et al., 1996, 2000; Mancktelow, 1999, 2001; Jeng et al., 2002). The adopted perturbation, the end-rotational method, involves the imposition of a boundary rotation with an angle θ, small in magnitude, at one end of the layer, as illustrated in Fig. 2. By employing this end-rotation, the shortened layer is applied a very small moment, which accounts for the subsequent buckle-folding. The rotation angle is small enough not to affect the yielding fold-forms. A typical range of rotation (θ) is about 5×10^{-1}–5×10^{-3} degree, within which range the bending cannot influence the development of waveforms and identical waveforms can be obtained.

For an elastic material, taking compression of a layer for example, stress will remain in a deformed system at the end of every step if external load is still applied on the boundary yet the boundary is not moving. However, for a viscous material, deviatoric stress will disappear at the end of a loading step, if the applied strain rate cannot be maintained to be non-zero at the end of step. Then compression of layer cannot cause buckling. Therefore, when the perturbation method is employed on the viscous system, minor modification to the applying procedures is made. The perturbation will be applied to the boundary at the beginning of the analysis, the system is then shortened to the pre-specified strain in one increment within the first step, and finally the system buckles, owing to this shortening and boundary perturbation, in later increments and steps.

3. Fold-forms at the moment of buckling

The fold-forms generated by the six layer–matrix system studied, are presented according to whether they are independent or dependent of strain rate of lateral compression.

3.1. Strain rate-independent cases (E–E, V–V)

3.1.1. E–E model

Since deformation of the elastic material is rate-independent, the fold-form is therefore rate-independent as (Currie et al., 1962; Jeng and Huang, 2008):

$$\varepsilon_x^B = \frac{\pi^2}{3l^2} + \frac{\overline{E}_o l}{2\pi\overline{E}} \tag{4}$$

where l is a normalized, dimensionless wavelength ($=L/h$); $\overline{E} = E/1-\nu^2$ and $\overline{E}_o = E_o/1-\nu_o^2$ are the equivalent Young's modulus of the layer and the matrix under a plane strain condition, respectively. For symbols and definitions of the theoretical solutions in Table 1, please refer to Jeng and Huang (2008).

Numerical analyses also confirm this rate-independent nature. As shown in Fig. 3, depending on the lateral compression when buckling occurs (ε_x^B), all the three types of fold-form can be

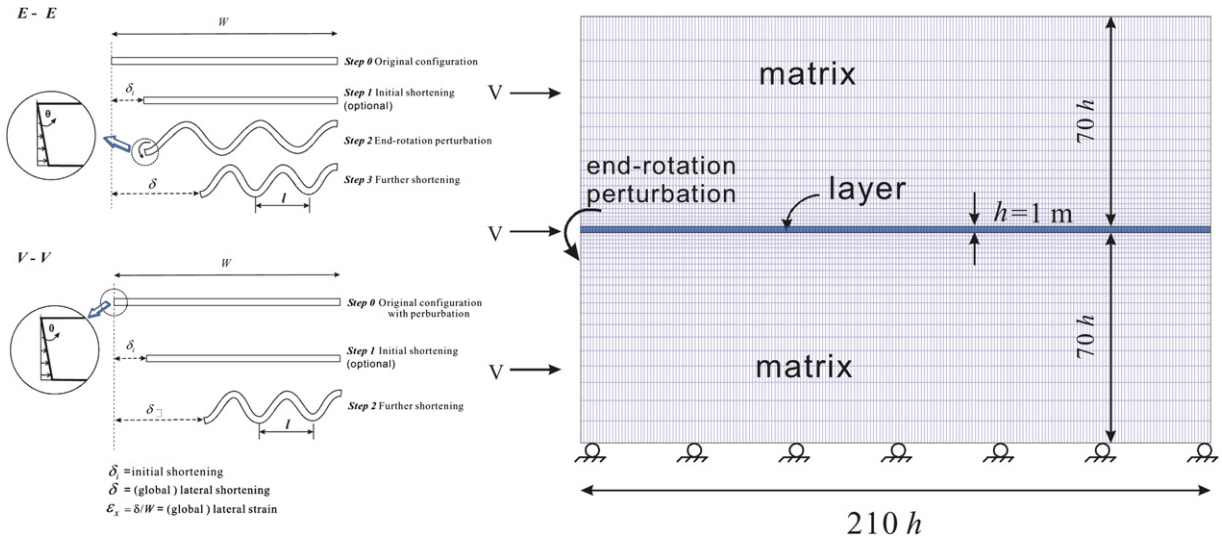

Fig. 2. Schematic illustration of end-rotation method adopted in numerical simulation. The perturbation is applied at the end of the competent layer by imposing a boundary displacement, with a rotation angle θ. For *E–E* model, an initial shortening (δ_i) was applied prior to end-rotation (*Step 1*), which accounts for the lateral compression before perturbation takes place. After end-rotation is applied, further lateral compression is then applied (*Step 3*) to trigger buckling of the layer–matrix system. For *V–V* model, the perturbation is applied before the beginning of analysis (*Step 0*), then the system is compressed to the initial shortening in one increment within the *Step 1* to induce buckling. Further shortening is applied (*Step 2*), subsequently.

a

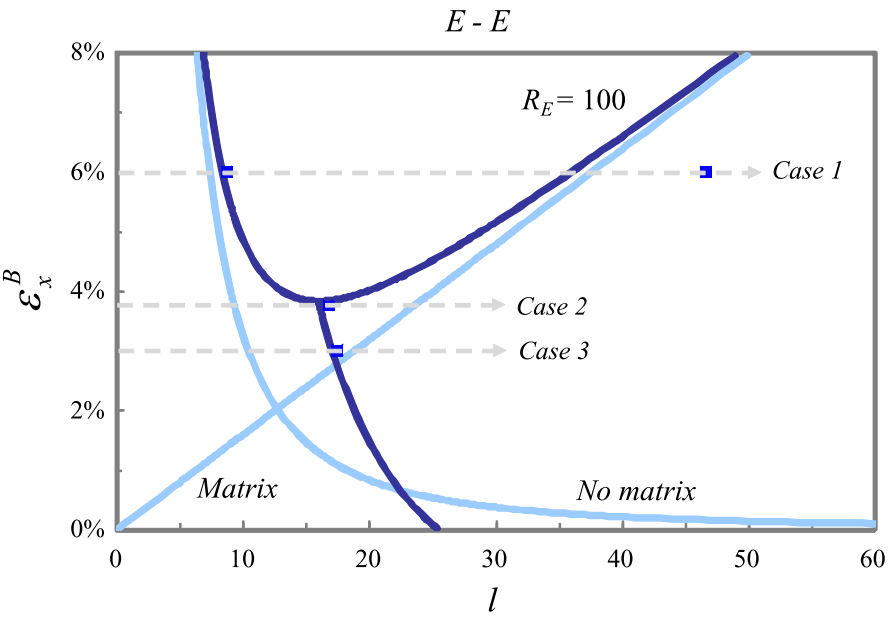

The $\varepsilon_x^B - l$ relationship for the *E*-*E* model

b

Case #	Type of fold-form	Resultant wavelength and fold-form
Case 1 $\varepsilon_x = 0.1$	***Type A***	$l_1 = 8.75$ $l_2 = 46.67$ $d = 1$
Case 2 $\varepsilon_x = 0.1$	***Type B***	$l_d = 16.8$ $d = 1$
Case 3 $\varepsilon_x = 0.037$	***Type C***	$l_3 = 17.5$ $d = 5$
Case 3	***Type C***	$l_3 = 17.5$ $d = 1$

The resultant fold-forms of each case

Fig. 3. The fold-forms obtained from the *E*–*E* model. The wavelengths l_1, l_2, l_d and l_3 are defined and illustrated in Fig. 1. The symbol ε_x is the amount of compression applied on the lateral boundaries. The theoretical solutions are indicated by the solid curves shown in Part (a). The wavelengths from numerical analyses are indicated by the symbols in Part (a), with corresponding fold-forms shown in Part (b). The input parameters are listed in Table 3. For this *E*–*E* model, $R_E = 100$. The symbol *d* denotes the magnification factor in *y*-direction for individual fold-form. The notation will also be adopted for rest of figures in this paper.

engendered. The resulting types of fold-form and the corresponding wavelengths are consistent with the predictions of theoretical solutions, as compared in Fig. 3a. Remarkably, upon a small amount of compression in the subsequent post-buckling stage, the *Type C* fold-form soon becomes *Type B* fold-form as shown by *Case 3* of Fig. 3b.

3.1.2. *V–V model*

Deformation of the viscous material is rate-dependent; however, the resulting fold-form is rate-independent as (Jeng and Huang, 2008):

$$\varepsilon_x^B = \frac{\pi^2}{3l^2} + \frac{\eta_o l}{2\eta\pi} \tag{5}$$

where η and η_o are the viscosity of the layer and the matrix, respectively.

This rate-independent nature is confirmed by numerical analysis. Two extreme strain rates have been applied (1×10^{-1} and $1 \times 10^{-15} s^{-1}$) and exactly same fold-forms are obtained. Similarly, depending on the lateral compression when buckling occurs (ε_x^B), three types of fold-form can be generated as shown in Fig. 4. The resulting types of fold-forms and the corresponding wavelengths are consistent with the prediction of theoretical solutions, as compared in Fig. 4a.

The *Type C* fold-form maintains its form during subsequent lateral compression in post-buckling stage; this folding behavior somewhat differs from that of *E*–*E* model, changing from *Type C* to *Type B*, as above-mentioned.

3.1.3. *Competency contrast R*

The folding behavior of strain rate-independent cases (*E*–*E*, *V*–*V* models) depend on the competence contrast *R* value and the

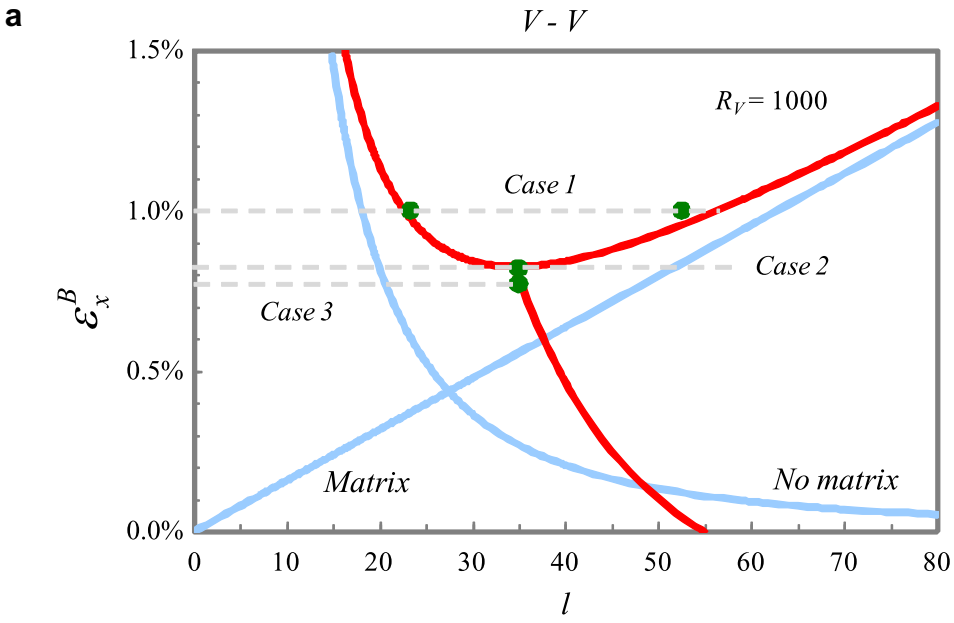

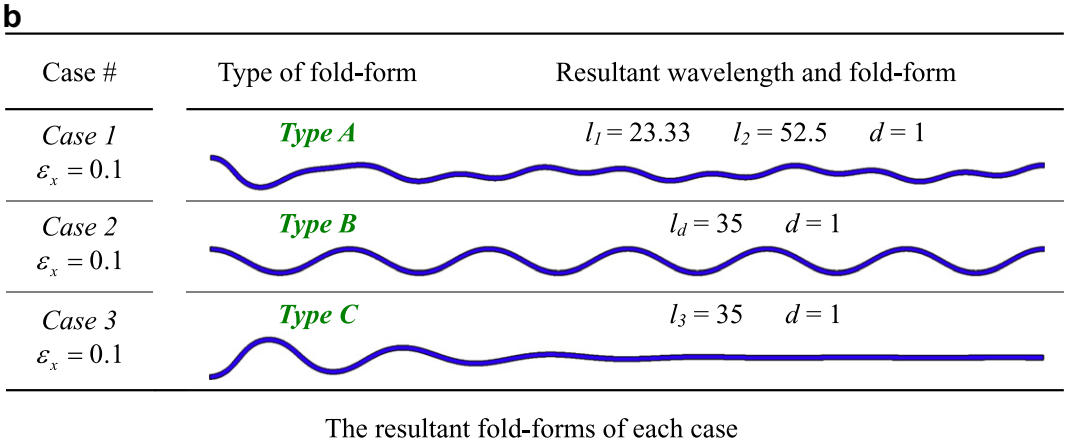

Fig. 4. The fold-forms obtained from the *V*–*V* model. The theoretical solutions are indicated by the curves shown in Part (a). The wavelengths from numerical analyses are indicated by the symbols in Part (a), with corresponding fold-forms shown in Part (b). The input parameters are listed in Table 3. For this *V*–*V* model, $R_V = 1000$. The magnification factor (d) is 1 for all fold-forms in this figure.

shortening strain while buckling. The fold-forms of *E*–*E* and *V*–*V* models, as indicated in Eqs. (4) and (5), can be expressed by a general form as:

$$\varepsilon_x^B = \frac{\pi^2}{3l^2} + \frac{l}{2R\pi} \tag{6}$$

where R represents the competence contrast of the system. For the *E*–*E* model, $R = R_E = \overline{E}/\overline{E}_o$ and for the *V*–*V* model, $R = R_V = \eta/\eta_o$. If there is no matrix, or equivalently R is approaching infinity, the term $l/2R\pi$ vanishes and the fold-form will solely be determined by the term $\pi^2/3l^2$. Therefore, the term $\pi^2/3l^2$ represents the system without matrix and is referred as "no matrix". On the other hand, the term $l/2R\pi$ represents the contribution of matrix to the formation of fold-form, and is referred as "matrix". These two terms are plotted in Figs. 3a and 4a.

Overall, the theoretical solutions indicate that, for rate-independent models, the resulting fold-forms only depend on R and ε_x^B, and the results of numerical analyses as shown in Figs. 3 and 4 confirm this prediction.

For higher competence contrast ($R \geq 100$), the numerical simulations agreed well with the theoretical solutions. At the same time, some previous researches pointed out that if the competence contrast is smaller than about 50 or even close to 10, then the thin-plate solution does not provide a good approximation and thick-plate solutions have to be used (Fletcher, 1974; Smith, 1975, 1977, 1979; Mühlhaus et al., 1994). Moreover, non-equilibrium thermodynamics has been used to obtain the fold-forms especially for low competence contrast situations (Hobbs et al., 2008). Therefore, this research also explored for what extent of competence ratio R the analytical one-dimension solutions are still valid. The competence contrast value of 50, 20 and 10 was adopted, respectively, and *Type A* and *Type B* fold-forms were numerical analyzed in the *E*–*E* model, and the results are shown in Fig. 5. Obviously, the numerical analysis results of *Type A* fold-form agree well with the theoretical solutions at high frequency. However, there is increasing inaccuracy at lower frequency as competence contrast R decreases. On the other hand, the numerical analysis results of *Type B* fold-form still agree well with the theoretical solutions. Overall, the numerical analyses show that, even with

a

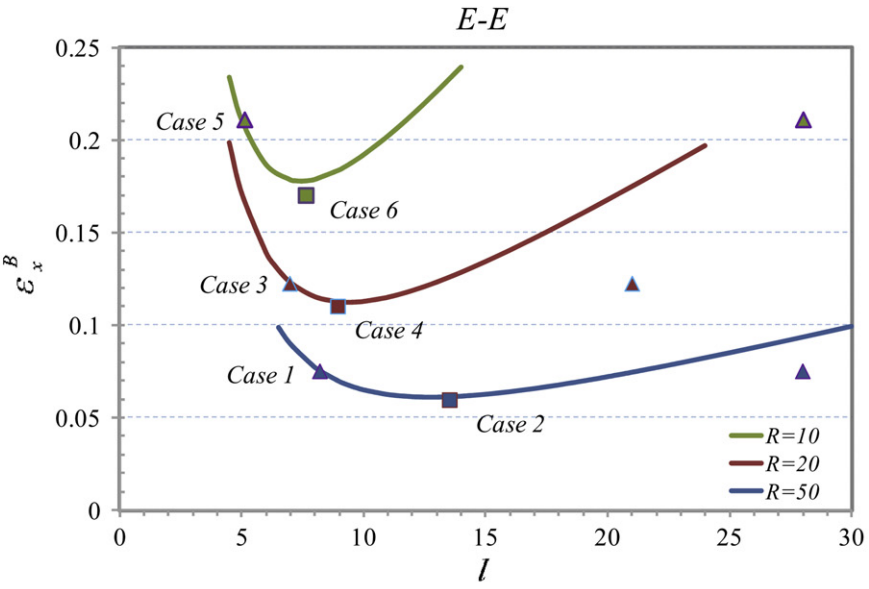

The $\varepsilon_x^B - l$ relationship for the *E-E* model

b

Case #	Type of fold-form	Resultant wavelength and fold-form
R=50 $\varepsilon_x = 0.08$	Case 1 **Type A**	$l_1 = 8.23$ $l_2 = 28$ $d = 1$
R=50 $\varepsilon_x = 0.07$	Case 2 **Type B**	$l_d = 13.55$ $d = 1$
R=20 $\varepsilon_x = 0.19$	Case 3 **Type A**	$l_1 = 7$ $l_2 = 21$ $d = 1$
R=20 $\varepsilon_x = 0.13$	Case 4 **Type B**	$l_d = 8.94$ $d = 1$
R=10 $\varepsilon_x = 0.29$	Case 5 **Type A**	$l_1 = 5.12$ $l_2 = 28$ $d = 1$
R=10 $\varepsilon_x = 0.18$	Case 6 **Type B**	$l_d = 7.64$ $d = 1$

The resultant fold-forms of each case

Fig. 5. The fold-forms of lower competence contrast obtained from the *E–E* model. The theoretical solutions are indicated by the curves shown in Part (a). The wavelengths from numerical analyses are indicated by the symbols in Part (a), with corresponding fold-forms shown in Part (b). The competence contrast values 50, 20 and 10 are adopted respectively. The magnification factor (d) is 1 for all fold-forms in this figure.

lower competence ratio, to some extent the analytical thin-plate one-dimension solutions are still valid.

3.2. Strain rate-dependent cases

3.2.1. EV–EV model

The fold-form of *EV–EV* model is related to strain rate as (Jeng and Huang, 2008):

$$\varepsilon_x^B = \frac{\pi^2}{3l^2} + \frac{\eta_\circ l\left(1 - e^{-\frac{T}{T_{Ro}}}\right)}{2\eta\pi\left(1 - e^{-\frac{T}{T_R}}\right)} \tag{7}$$

where T_R and T_{Ro} are the relaxation time of the layer and the matrix, and are defined as $T_R = \eta/G$ and $T_{Ro} = \eta_o/G_o$, respectively.

When the strain rate is very fast, the folding behavior will convert to *E–E* model as:

$$\varepsilon_x^B = \lim_{T\to 0}\frac{\pi^2}{3l^2}+\frac{l\left(1-e^{-\frac{T}{T_{Ro}}}\right)}{2R_V\pi\left(1-e^{-\frac{R_E}{R_V}\frac{T}{T_{Ro}}}\right)} = \frac{\pi^2}{3l^2}+\frac{l}{2R_E\pi} \quad (8)$$

When the strain rate is very slow, the folding behavior will convert to *V–V* model as:

$$\varepsilon_x^B = \lim_{T\to\infty}\frac{\pi^2}{3l^2}+\frac{l\left(1-e^{-\frac{T}{T_{Ro}}}\right)}{2R_V\pi\left(1-e^{-\frac{R_E}{R_V}\frac{T}{T_{Ro}}}\right)} = \frac{\pi^2}{3l^2}+\frac{l}{2R_V\pi} \quad (9)$$

In order to distinguish the influence of R_E and R_V, these two competence contrasts are deliberately set to be 100 and 1000, as summarized in Table 3.

a

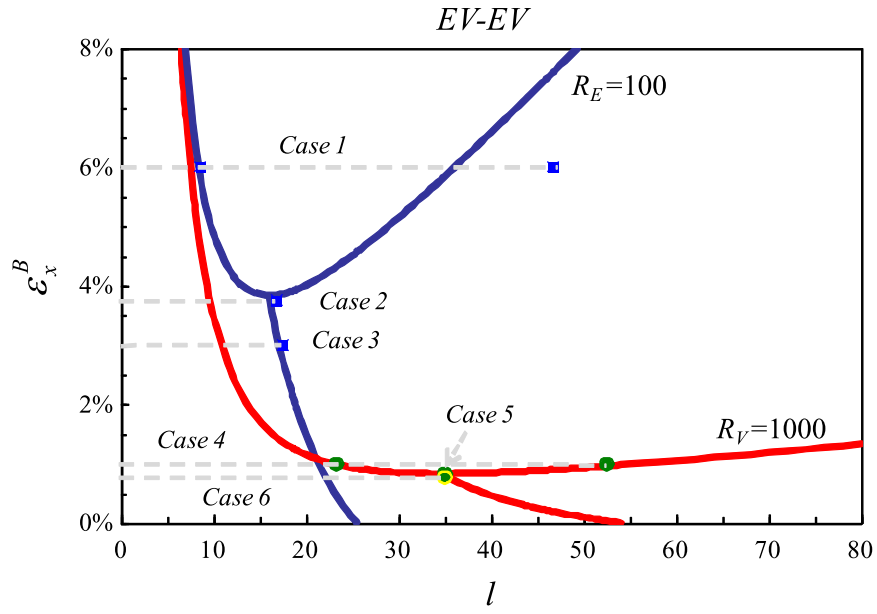

The $\varepsilon_x^B - l$ relationship for the *EV-EV* model

b

Case #	Type of fold-form	Resultant wavelength and fold-form
Case 1 $\varepsilon_x = 0.1$	***Type A*** $\dot{\varepsilon}_x = 0.1$	$l_1 = 8.75$ $l_2 = 46.67$ $d = 1$
Case 2 $\varepsilon_x = 0.1$	***Type B*** $\dot{\varepsilon}_x = 0.1$	$l_d = 16.8$ $d = 1$
Case 3 $\varepsilon_x = 0.1$	***Type C*** $\dot{\varepsilon}_x = 0.1$	$l_3 = 17.5$ $d = 1$
Case 4 $\varepsilon_x = 0.1$	***Type A*** $\dot{\varepsilon}_x = 1\times10^{-15}$	$l_1 = 23.33$ $l_2 = 52.5$ $d = 1$
Case 5 $\varepsilon_x = 0.1$	***Type B*** $\dot{\varepsilon}_x = 1\times10^{-15}$	$l_d = 35$ $d = 1$
Case 6 $\varepsilon_x = 0.1$	***Type C*** $\dot{\varepsilon}_x = 1\times10^{-15}$	$l_3 = 35$ $d = 1$

The resultant fold-forms of each case

Fig. 6. The fold-forms obtained from the *EV–EV* model. *Cases 1–3* are obtained using very fast strain rate, $\dot{\varepsilon}_x = 1\times10^{-1}s^{-1}$. *Cases 4–6* are obtained using very slow strain rate, $\dot{\varepsilon}_x = 1\times10^{-15}s^{-1}$. The solid curves with dark and light colors and are theoretical solutions of the *E–E* and *V–V* models, respectively. The magnification factor (d) is 1 for all fold-forms in this figure.

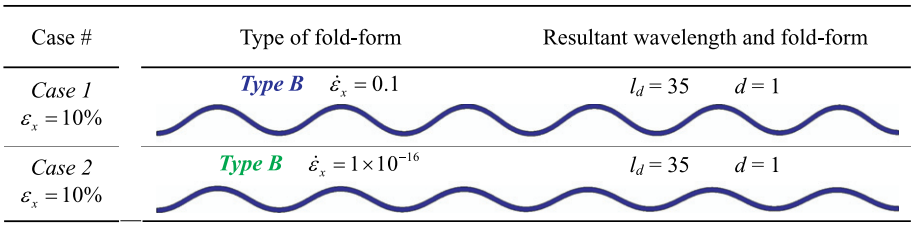

Fig. 7. The fold-forms of the *EV–EV* model with $R_E = R_V = 1000$. Strain rates for *Case 1* and *Case 2* are 1×10^{-1} and 1×10^{-16} s^{-1}, respectively. The magnification factor (d) is 1 for all fold-forms in this figure.

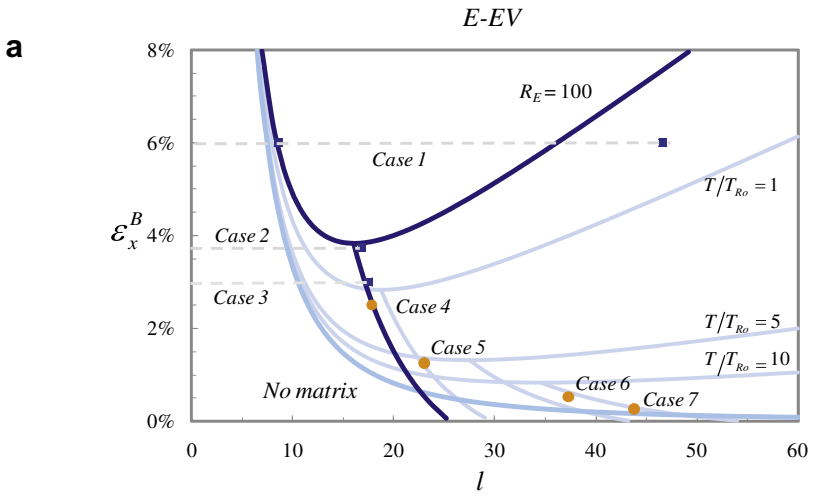

b The $\varepsilon_x^B - l$ relationship for *E-EV* model

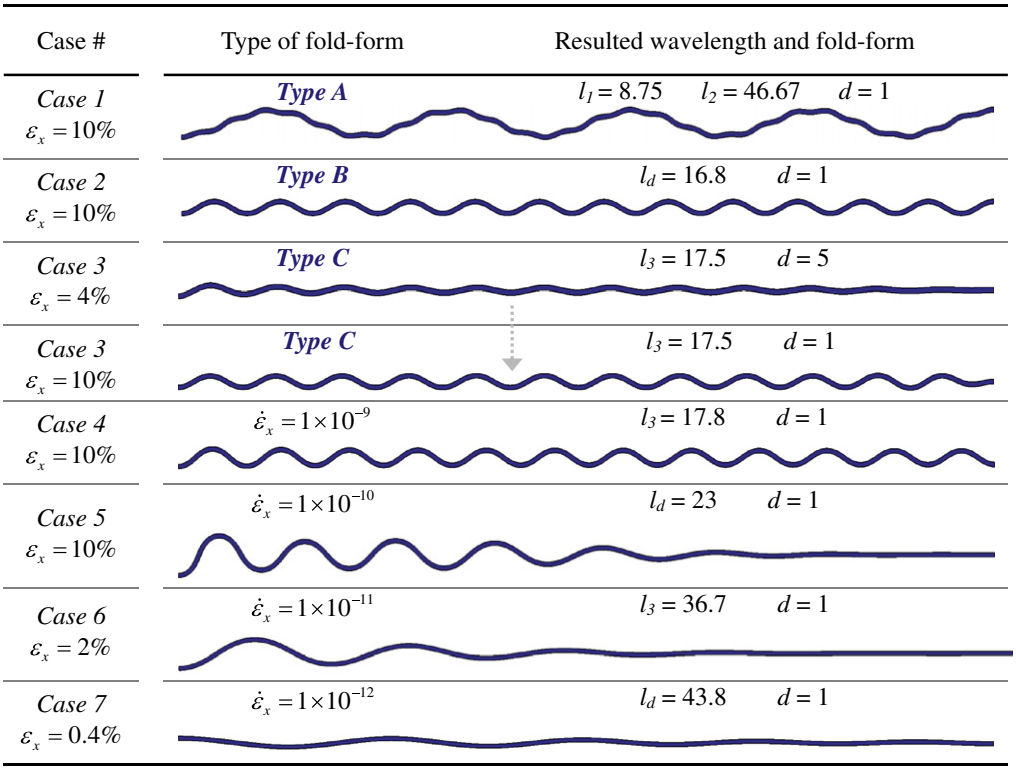

The resulted fold-forms of each case

Fig. 8. The fold-forms of the *E–EV* model. *Cases 1–3* are obtained with very fast strain rate, $\dot{\varepsilon}_x = 1\times10^{-1}s^{-1}$. The strain rates for *Cases 4–7* are 1×10^{-9}, 1×10^{-10}, 1×10^{-11}, 1×10^{-12} s^{-1}, respectively. The magnification factor (d) is 1 for all fold-forms in this figure. $T_{Ro} = (\eta_o/G_o) = 1\times10^7$ s for this case.

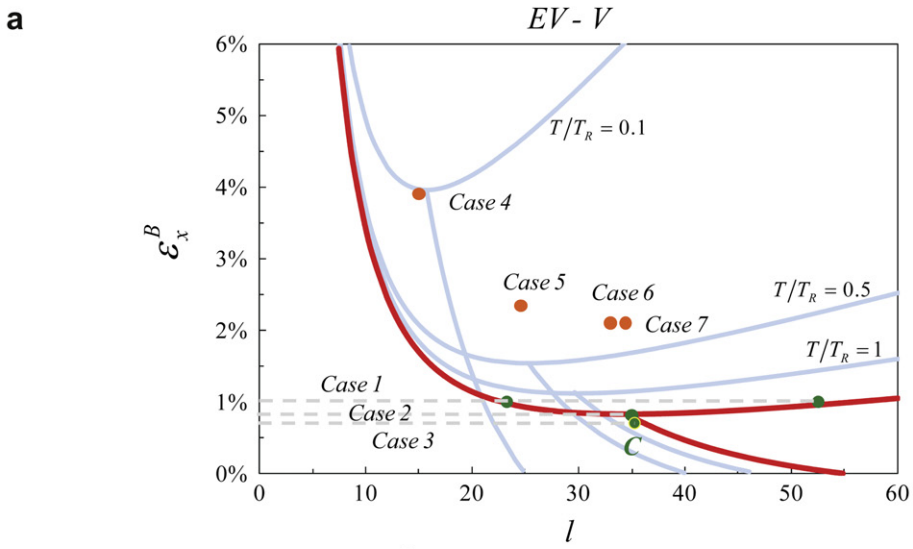

The $\varepsilon_x^B - l$ relationship for the *EV-V* model

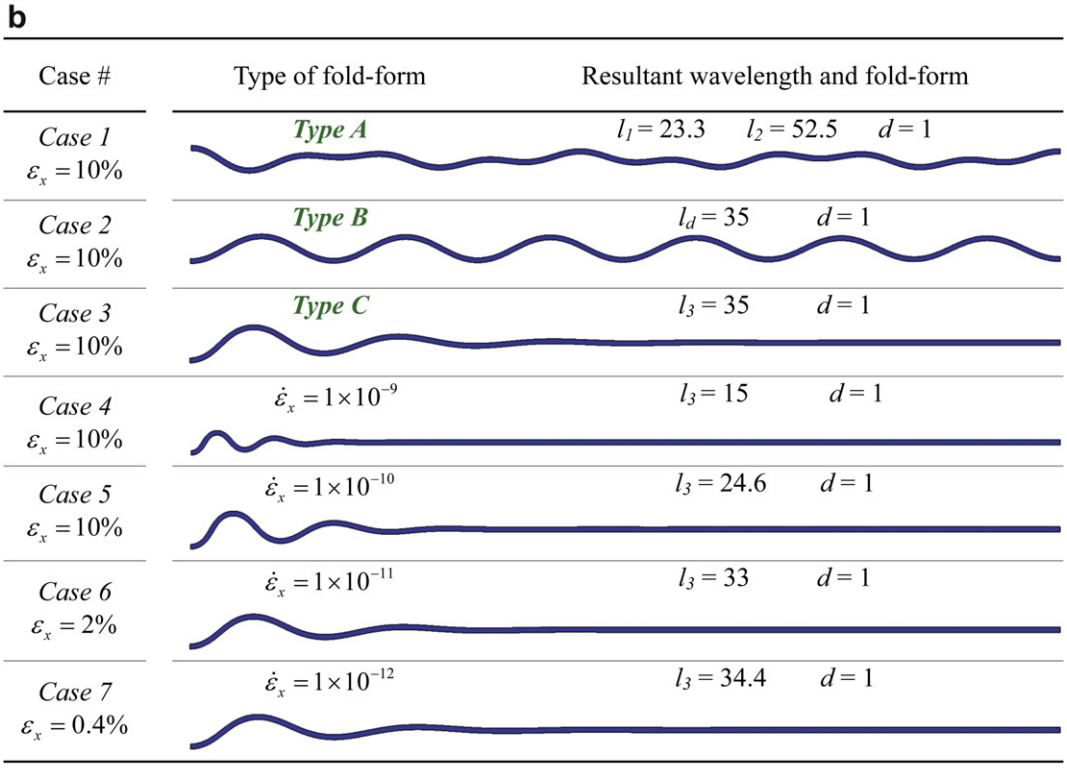

The resultant fold-forms of each case

Fig. 9. The fold-forms of the *EV–V* model. *Cases 1–3* are obtained with very slow strain rate, $\dot{\varepsilon}_X = 1\times10^{-15}\ s^{-1}$. The strain rates for *Cases 4–7* are 1×10^{-9}, 1×10^{-10}, 1×10^{-11}, $1\times10^{-12}\ s^{-1}$, respectively. The magnification factor (d) is 1 for all fold-forms in this figure. $T_R = (\eta/G) = 1\times10^8$ s for this case.

The numerical analyses results confirm the folding behavior of *EV–EV* model under extreme strain rates, as shown in Fig. 6. Under extreme fast strain rate, the resulting wavelengths compared well with the theoretical solutions of *E–E* model, marked as the square symbols shown in Fig. 6a. On the other hand, under extreme slow strain rate, the resulted wavelengths match the predictions of *V–V* model, marked as the circular symbols shown in Fig. 6a. The three types of fold-forms can be generated depending on the applied strain rate and ε_x^B.

In the special case, $R_E = R_V$, the resulting fold-form will convert from Eqs. (8) and (9) to Eq. (6) so that the *EV–EV* model becomes rate-independent. The numerical results confirm this particular behavior as shown in Fig. 7. As $R_E = R_V = 1000$, the same fold-forms are obtained by two strain rates significantly differing with each other with the order of 15, as shown in Fig. 7. In these two cases, both *Type B* fold-forms with same wavelength are obtained, except that the amplification of fold-amplitude of *V–V* model is somewhat smaller in the later post-buckling stage. It should be noted that the theoretical solutions focus on the moment of buckling but may not necessarily be applicable to the folding behavior in the subsequent post-buckling stage.

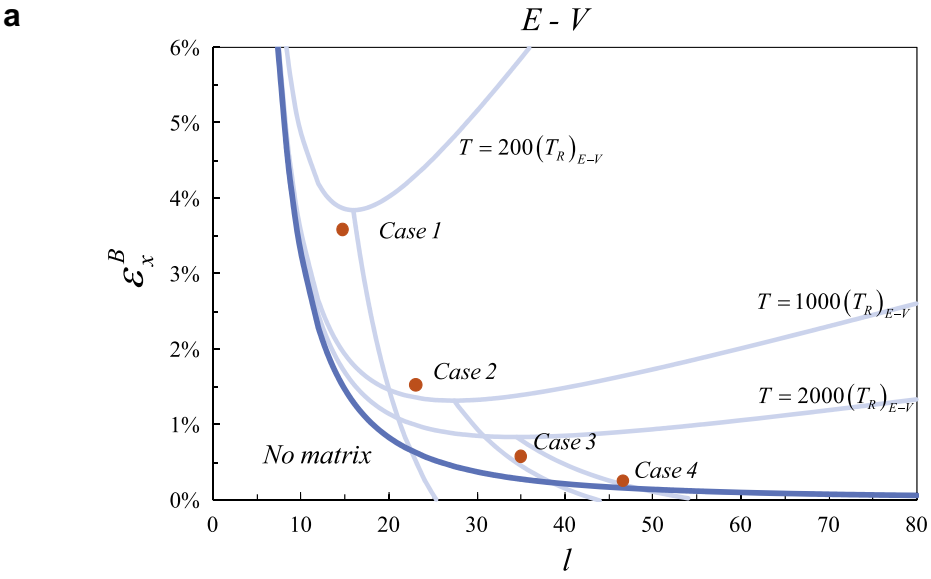

The $\varepsilon_x^B - l$ relationship for the *E-V* model

b

Case #	Type of fold-form	Resultant wavelength and fold-form
Case 1 $\varepsilon_x = 10\%$	$\dot{\varepsilon}_x = 1\times10^{-9}$	$l_3 = 14.8$ $d = 1$
Case 2 $\varepsilon_x = 10\%$	$\dot{\varepsilon}_x = 1\times10^{-10}$	$l_3 = 23.1$ $d = 1$
Case 3 $\varepsilon_x = 1\%$	$\dot{\varepsilon}_x = 1\times10^{-11}$	$l_3 = 35$ $d = 1$
Case 4 $\varepsilon_x = 0.5\%$	$\dot{\varepsilon}_x = 1\times10^{-12}$	$l_3 = 46.7$ $d = 1$

The resultant fold-forms of each case

Fig. 10. The fold-forms of the *E–V* model. The strain rates for *Cases 1–4* are 1×10^{-9}, 1×10^{-10}, 1×10^{-11}, 1×10^{-12} s^{-1}, respectively. The magnification factor (d) is 1 for all fold-forms in this figure. $(T_R)_{E-V} = \eta_o/\overline{G}$, $\overline{G} = G/1-\nu$, and $(T_R)_{E-V} = 5\times10^4$ s.

This validation provides an important message, that in order to explore the impact of the strain rate to *EV–EV* system, one must set different competence contrast to elastic and viscous properties (i.e. $R_E \neq R_V$).

3.2.2. *E–EV model*

On the basis of theoretical solution, the *E–EV* model converts to the *E–E* model as strain rate is very fast. Numerical results as shown in Fig. 8 confirm this behavior. As shown by *Cases 1–3* in Fig. 8, the resulting fold-forms (type and wavelength) compare with of the corresponding *E–E* model, in which all three types of fold-form are possible.

When the applied strain is not very fast, the applied strain rates can affect the fold-forms, as shown by *Cases 4–7* in Fig. 8. Remarkably, for *Cases 4–7*, only *Type C* fold-form is obtained. The end-perturbation which is employed at the beginning of lateral compression may account for the early occurrence of folding (earlier than *Type B* fold-form) so that *Type C* fold is obtained. When the applied strain rate becomes slower, the resulting fold-form gets closer to the "no matrix" curve, as shown in Fig. 8.

3.2.3. *EV–V model*

On the basis of theoretical solution, the *EV–V* model converts to the *V–V* model as strain rate is very slow. Numerical results as shown in Fig. 9 confirm this behavior. As shown by *Cases 1–3* in Fig. 9, the resulting fold-forms (type and wavelength) compare with of the corresponding *V–V* model, in which all three types of fold-form are possible.

When the applied strain is not very slow, the applied strain rates can affect the fold-forms, as shown by *Cases 4–7* in Fig. 9. Similarly, for *Cases 4–7*, only *Type C* fold-form is obtained. The end-perturbation which is employed at the beginning of lateral compression may account for the early folding (earlier than *Type B* fold-form) so that *Type C* fold is accordingly obtained. When the applied strain rate becomes slower, the resulting fold-form gets closer to the *V–V* curve, as shown in Fig. 9.

3.2.4. *E–V model*

The results of numerical simulations indicate that the fold-forms of the *E–V* model are affected by the applied strain rates, as shown in Fig. 10. This strain rate-dependent nature of the *E–V*

model agrees with the theoretical predictions by Jeng and Huang (2008), yet differs from the rate-independent prediction by Biot (1961). This phenomenon is also discussed in a different way in previous research (Hunt et al., 1996a; Schmalholz and Podladchikov, 1999). Similarly, for *Cases 1–4*, only *Type C* fold-form is obtained due to the end-perturbation which is employed at the beginning lateral compression. When the applied strain rate becomes slower, the resulting fold-form gets closer to the "no matrix" curve, as shown in Fig. 10.

3.2.5. Summary

The four models studied in this section are rate-dependent in general, except in the situation that the effect of strain rate is compensated by letting $R_E = R_V$ in the *EV–EV* model. Overall, the resulting fold-forms agree well with the theoretical predictions, including rate-dependency, type of fold-form and wavelength.

All three types of fold-form can be generated, as long as the applied strain rate approaches the boundaries of the *E–E* or *V–V* models. On the other hand, when the *V–V* model is not the lower boundary of fold-forms, the "no matrix" curve becomes the lower boundary of the fold-forms. In such a situation, *Type C* will often be generated, which can possibly be accounted for by the fact that the end-perturbation is employed right at the beginning of lateral compression. Meanwhile, a slower strain rate will bring the fold-form closer to the one dominated by the "no matrix" curve.

It is hard to estimate geological conditions by the fold formation. Even though the material properties of layer and matrix can be known, still one cannot estimate strain rate and shortening strain while buckling. Due to this analysis, nevertheless, how the strain rate and shortening strain while buckling affects the fold-form generation can be preliminarily understood.

4. Folding behavior in the post-buckle stage

The subsequent deformation of fold in the post-buckling stage is beyond the ability of the proposed theoretical solutions. A dimensionless measure based on relaxation time of the layer–matrix system has been proposed to indicate whether the strain rate is fast or slow (Jeng and Huang, 2008). Since numerical simulations are able to yield results agreeing well with theoretical solutions at the buckling stage, the validity of both theoretical solutions and numerical simulation adopted in this research seems to be well supported. Therefore, the folding behavior in post-buckling stage is further studied by observing the folding behavior revealed by numerical simulation.

Systematic study on the post-buckling behavior of all six models has been conducted. It was found that the post-buckling behavior of the *E–E* and *V–V* models are most representative; as to other four models, their behaviors range within the behaviors of these two models in most cases, except for *Type C* fold-forms. Therefore, the post-buckling behavior of the *E–E* and *V–V* models for three types of fold-forms are presented first. The variations of *Type C* fold-forms obtained from the other four models are then presented.

4.1. Elastic folding versus viscous folding

Although these two models share same general fold-form (Eq. (6)) at the buckling stage, discrepancies exit in their post-buckling behavior.

4.1.1. Type A fold-form

For dual-frequency fold-form (*Type A*), the process of post-buckling deformation yielded by elastic folding (*E–E*, *E–EV*, *EV–EV* models) is shown in Fig. 11. A dual-frequency fold-form is initiated

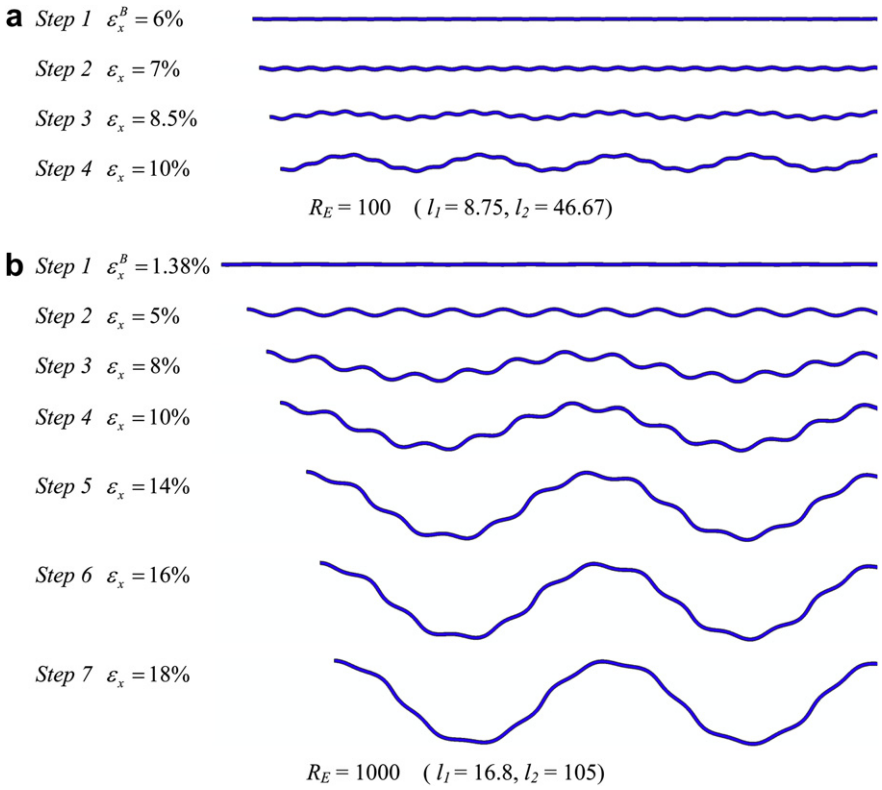

Fig. 11. Variation of *Type A* fold-form during post-buckling deformation of elastic folding (*E–E* model). The R_E for the cases in Parts (a) and (b) are 100 and 1000, respectively. The ε_x^B for the two cases are 6.0% and 1.38%, respectively. The symbols, l_1 and l_2, are the wavelengths right after buckling. The magnification factor (d) is 1 for all fold-forms in this figure.

at the moment of buckling, yet the magnitude is often rather small, as shown in *Step 1* of Fig. 11a, so that it cannot be recognized if the amplitude is not magnified. Using fast Fourier transform (FFT), the dual wavelengths can be revealed as shown in Fig. 12a. Although, the amplitudes of these two frequencies are not clearly visible (*Step 1* in Fig. 11a), the result of FFT, in which frequency has been converted into wavelength for convenience, clearly indicates the existence of two frequencies, as shown in Fig. 12a. Remarkably, by observing the relative amplitudes of the dual-frequency fold-form, it is found that the higher frequency (l_1) has much greater amplitude than the lower frequency (l_2).

While continuing compression shortly after buckling, the amplitude of the higher frequency (l_1) in the dual-frequency fold-form is first amplified, as shown in *Step 2* of Fig. 11a. Next the amplitude of the lower frequency (l_2) is then amplified, as shown in *Step 3*. Finally, when the amplitude of the lower frequency becomes much larger than that of higher frequency, the amplitude of the fold-form of the higher frequency seems to be stretched down by the fold-form of the lower frequency, and somewhat diminishes, as shown in *Step 4* in Fig. 11a. As shown in Fig. 12b, fast Fourier transform of the fold-form (in *Step 4*) indicates that the amplitude of l_2 becomes much greater than that of l_1. It is noticeable that, as revealed by numerical simulation, the relative amplitude of the dual-frequencies can be significantly changed during the process of folding. A further study regarding how and why these frequencies are changed is needed to perceive the underlain mechanism. A similar post-buckling deformation can be observed for $R_E = 100$ (Fig. 11a) and $R_E = 1000$ (Fig. 11b).

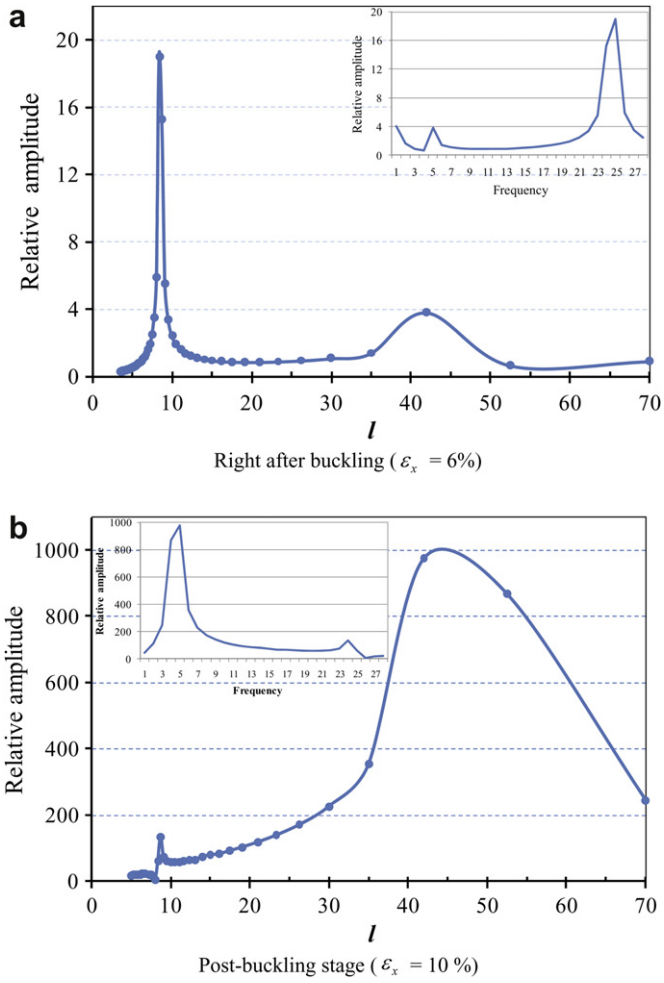

Fig. 12. Fast Fourier transform of fold-forms shown in Fig. 11a. Parts (a) and (b) correspond to *Step 1* and *Step 4* in Fig. 11a, respectively. Frequencies have been converted to wavelengths for convenience. The original result of FFT is also attached in the each figure.

For viscous folding (*EV–EV*, *EV–V*, *V–V* models), dual-frequency occurs at the moment of buckling although it is not readily visible without magnification, as shown in *Step 1* of Fig. 13a. The amplification of high frequency occurs first, just as the *E–E* model, as shown in *Step 2* of Fig. 13a. Nevertheless, the later amplified lower frequency does not markedly stretch the higher frequency fold-form, so that both of the dual-frequencies remain in the later stages of deformation, as shown in Fig. 13a. A similar post-buckling deformation can be obtained for $\varepsilon_x^B = 1.0\%$ (Fig. 13a) and $\varepsilon_x^B = 1.38\%$ (Fig. 13b). Remarkably, as shown in Fig. 13b, the severe distortion of the fold near the left-end at the final step of deformation is possibly caused by the local initial end-perturbation applied on the left-end.

The dual-frequency fold-form is similar to the two order folds, interpreted by Price and Cosgrove (1990). The amplifying process of the higher frequency and the lower frequency fold-forms is very similar to the interpretation of the first order and the second order folds by Price and Cosgrove (1990). The only difference is that the dual-frequency fold-form has been triggered simultaneously at the moment of buckling, as revealed by theoretical solutions (Jeng and Huang, 2008) and numerical simulation of this research. To clarify why the higher frequency is first amplified, a further study is required. On the other hand, to confirm this phenomenon in outcrop is hard. Both the single frequency fold-form and dual-frequency fold-form can be found in outcrop; supporting the proposition of Price and Cosgrove (1990); nevertheless, they seem not to negate the observation of this research.

4.1.2. Type B fold-form

If *Type B* fold-form is formed at buckling, the subsequent lateral compression seems only to shorten the wavelength and magnify the amplitude, without changing the type of fold-form, for both elastic folding (*E–E*, *E–EV*, *EV–EV* models) and viscous folding (*EV–EV*, *EV–V*, *V–V* models). Furthermore, the second order fold is not observed in later stages of post-buckling deformation. As far as revealed by numerical analyses, the second order fold can occur only when dual-frequency fold is formed at the moment of buckling.

4.1.3. Type C fold-form

Type C fold-form yielded by elastic folding (*E–E*, *E–EV*, *EV–EV* models) swiftly changes to similar *Type B* in post-buckling stage, as shown in *Case 3* of Fig. 4. Yet, for viscous folding (*EV–EV*, *EV–V*, *V–V* models), the amplitude of *Type C* fold-form is sequentially magnified from the perturbed end toward the decaying end in a relatively slower manner. Upon significant amount of post-buckling deformation, the original *Type C* fold-form of viscous folding becomes closer to *Type B* fold-form. Overall, *Type C* fold-form of viscous folding (*EV–EV*, *EV–V*, *V–V* models), together with the *E–EV* and *E–V* models under very slow strain rates, can exist for a rather long period during post-buckling deformation. This phenomenon implies that the *Type C* fold-form observed in outcrop should be formed and subsequently deformed within a rather "viscous" environment, or under a rather slow strain rate.

4.2. Variation of Type C fold-forms yielded by other models

For the models (*EV–EV* and *EV–V*) which have the *V–V* model as their lower bound upon very slow strain rate, the variations of *Type C* fold-form in post-buckling stage are quite similar to those of the *V–V* model: the amplitude of *Type C* fold-form is sequentially magnified from the perturbed end toward the decaying end in

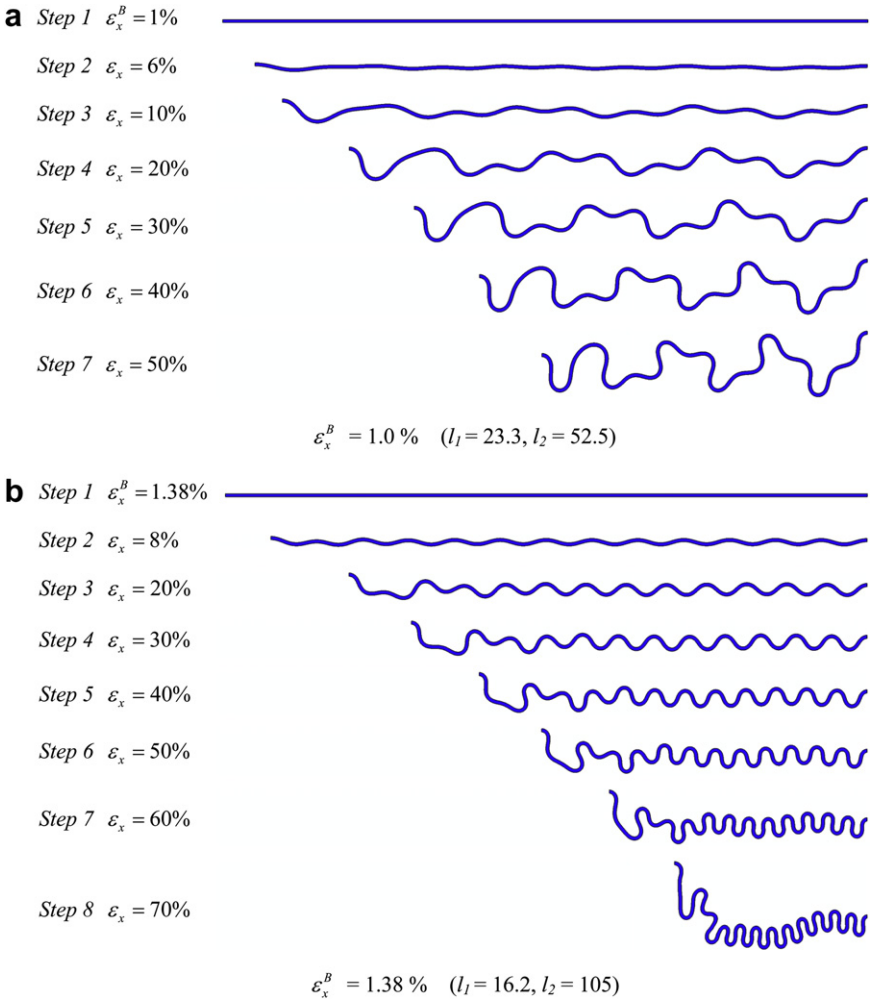

Fig. 13. Variation of *Type A* fold-form during post-buckling deformation of viscous folding (*V*–*V* model). The R_V is 1000 for both cases. The ε_x^B for the cases in Parts (a) and (b) are 1.0% and 1.38%, respectively. The symbols, l_1 and l_2, are the wavelengths right after buckling. The magnification factor (*d*) is 1 for all fold-forms in this figure.

a relatively slower manner. If medium strain rates are applied, it is found that a slower strain leads to a greater wavelength of *Type C* fold. If the strain rate is very slow, the folding behavior is then controlled by the *V*–*V* model again.

For the models (*E*–*EV* and *E*–*V*) in which the no matrix curve, instead of the *V*–*V* model, serves as the lower bound, the original *Type C* fold-forms can be changed, both wavelength and amplitude are unevenly and significantly changed within the layer–matrix system during the post-buckling stage. It is extremely difficult to categorize the type of fold-forms.

5. Closing remarks

Numerical simulation can imitate the folding process. The phenomena that the fold-forms predicted by theoretical solutions and resulting from numerical analyses are in good agreement indicate that: (1) in most ranges of contrast, the analytical solutions are representative of two-dimensional buckle-folding; (2) the simplified one-dimensional governing equations can keep the characteristics of two-dimensional numerical simulation; (3) last but not least, the validity and the performance of numerical analysis itself seem to be also acceptable.

Beyond the capacity of those analytical solutions, designated only for the moment of buckling, the post-buckling folding behavior for elastic folding and viscous folding has been presented based on numerical analyses. It can be seen that, in additional to the shortening of original wavelength and amplifying of original amplitude at buckling, the fold-form can be significantly altered in some situations, as presented in previous sections.

It is wished to observe folding behavior at even greater degree of lateral compression. However, too severe distortion of mesh would prevent convergence of numerical computation so that some simulations will be terminated at medium range of shortening (40–60%), even less than 20% for elastic folding. More technology for the numerical analysis should be employed in a further study to achieve this purpose.

Acknowledgements

The authors thank Tom Blenkinsop and Stefan Schmalholz for comments that greatly improved this paper. The anonymous reviewer who offered exceedingly constructive comments is also thanked. This research is partially supported by the National Science Council of Taiwan, Contract No. 97-2116-M-002-015 and 98-2811-M-002-068.

References

Abbassi, M.R., Mancktelow, N.S., 1990. The effect of initial perturbation shape and symmetry on fold development. Journal of Structural Geology 12, 273–282.

Abbassi, M.R., Mancktelow, N.S., 1992. Single layer buckle in non-linear material – I. Experimental study of fold development from an isolated initial perturbation. Journal of Structural Geology 14, 85–104.
Biot, M.A., 1957. Folding instability of a layered viscoelastic medium under compression. Proceedings of the Royal Society of London. Series A, Mathematical and Physical Sciences 242, 444–454.
Biot, M.A., 1959. Folding of a layered viscoelastic medium derived from an exact stability theory of a continuum under initial stress. Quarterly of Applied Mathematics 17, 185–204.
Biot, M.A., 1961. Theory of folding of stratified viscoelastic media and its implications in tectonics and orogenesis. Geological Society of America Bulletin 72, 1595–1620.
Biot, M.A., Odé, H., Roever, W.L., 1961. Experimental verification of the theory of folding of stratified viscoelastic media. Geological Society of America Bulletin 72, 1621–1632.
Chapple, W.M., 1968. A mathematical theory of finite-amplitude rock folding. Geological Society of America Bulletin 79, 47–68.
Chapple, W.M., 1969. Fold shape and rheology: the folding of an isolated viscous-plastic layer. Tectonophysics 7, 97–116.
Cobbold, P.R., 1975. Fold propagation in single embedded layers. Tectonophysics 27, 333–351.
Cobbold, P.R., 1976. Fold shapes as functions of progressive strain. Philosophical Transactions of the Royal Society of London A 283, 129–138.
Cobbold, P.R., 1977. Finite-element analysis of fold propagation – a problematic application? Tectonophysics 38, 339–353.
Currie, J.B., Patnode, H.W., Trump, R.P., 1962. Development of folds in sedimentary strata. Geological Society of America Bulletin 73, 655–674.
Dieterich, J.H., Carter, N.L., 1969. Stress history of folding. American Journal of Science 267, 129–154.
Donath, F.A., Parker, R.B., 1964. Folds and folding. Geological Society of America Bulletin 75, 45–62.
Druguet, E., Alsop, G.I., Carreras, J., 2009. Coeval brittle and ductile structures associated with extreme deformation partitioning in a multilayer sequence. Journal of Structural Geology 31, 498–511.
Dubey, A.K., Cobbold, P.R., 1977. Noncylindrical flexural slip folds in nature and experiment. Tectonophysics 38, 223–239.
Fletcher, R.C., 1974. Wavelength selection in the folding of a single layer with power-law rheology. American Journal of Science 274, 1029–1043.
Fletcher, R.C., 1977. Folding of a single viscous layer: exact infinitesimal-amplitude solution. Tectonophysics 39, 593–606.
Hobbs, B.E., 1971. The analysis of strain in folded layers. Tectonophysics 11, 329–375.
Hobbs, B.E., Regenauer-Lieb, K., Ord, A., 2008. Folding with thermal–mechanical feedback. Journal of Structural Geology 30, 1572–1592.
Hudleston, P.J., 1973a. Fold morphology and some geometrical implications of theories of fold development. Tectonophysics 16, 1–46.
Hudleston, P.J., 1973b. An analysis of "single-layer" folds developed experimentally in viscous media. Tectonophysics 16, 189–214.
Hudleston, P.J., Stephansson, O., 1973. Layer shortening and folding shape development in the buckling of single layers. Tectonophysics 17, 299–321.
Hudleston, P.J., 1986. Extracting information from folds in rocks. Journal of Geological Education 34, 237–245.
Hudleston, P.J., Lan, L., 1993. Information from fold shapes (in: Special Issue—'Geometry of Naturally Deformed Rocks'). Journal of Structural Geology 15, 253–264.
Hudleston, P.J., Lan, L., 1994. Rheological controls on the shapes of single-layer folds. Journal of Structural Geology 16, 1007–1021.
Hudleston, P.J., Treagus, S., Lan, L., 1996. Flexural flow: does it occur in nature? Geology 24, 203–206.
Hunt, G.W., Mühlhaus, H.B., Whiting, A.I.M., 1996a. Evolution of localized folding for a thin elastic layer in a softening visco-elastic medium. Pure and Applied Geophysics 146, 229–252.
Hunt, G.W., Mühlhaus, H.B., Hobbs, B.E., Ord, A., 1996b. Localized folding of viscoelastic layers. Geologische Rundschau 85, 58–64.
Jeng, F.S., Lu, C.Y., Chang, N.G., 2001. Buckle folding of elastic strata. Proceedings of 10th International Conference on Computer Methods and Advances in Geomechanics, Tucson, USA, pp. 1309–1312.
Jeng, F.S., Lai, Y.C., Teng, M.H., 2002. Influence of strain rate on buckle folding of an elasto-viscous single layer. Journal of Structural Geology 24, 501–516.
Jeng, F.S., Huang, K.P., 2008. Buckling folds of a single layer embedded in matrix – theoretical solutions and characteristics. Journal of Structural Geology 30, 633–648.
Johnson, A.M., Fletcher, R.C., 1994. Folding of Viscous Layers. Columbia University Press, New York.
Karman, T.V., Biot, M.A., 1940. Mathematical Methods in Engineering. Mcgraw-Hill, New York.
Kocher, T., Mancktelow, N.S., Schmalholz, S.M., 2008. Numerical modelling of the effect of matrix anisotropy orientation on single layer fold development. Journal of Structural Geology 30, 1013–1023.
Lan, L., Hudleston, P.J., 1991. Finite element models of buckle folds in non-linear materials. Tectonophysics 199, 1–12.
Lan, L.B., Hudleston, P.J., 1996. Rock rheology and sharpness of folds in single layers. Journal of Structural Geology 18, 925–931.
Latham, J.-P., 1985a. The influence of nonlinear material properties and resistance to bending on the development of internal structures. Journal of Structural Geology 7, 225–236.
Latham, J.-P., 1985b. A numerical investigation and geological discussion of the relationship between folding, kinking and faulting. Journal of Structural Geology 7, 237–249.
Mancktelow, N.S., Abbassi, M.R., 1992. Single layer buckle folding in non-linear materials – II. Comparison between theory and experiment. Journal of Structural Geology 14, 105–120.
Mancktelow, N.S., 1999. Finite-element modelling of single-layer folding in elasto-viscous materials: the effect of initial perturbation geometry. Journal of Structural Geology 21, 161–177.
Mancktelow, N.S., January 2001. Single-layer folds developed from initial random perturbations: the effects of probability distribution, fractal dimension, phase and amplitude. Geological Society of America Memoir 193, 69–87.
Mühlhaus, H.-B., Hobbs, B.E., Ord, A., 1994. The role of axial constraints on the evolution of folds in single layers. In: Siriwardane, Zaman (Eds.), Computer Methods and Advances in Geomechanics. Balkema, Rotterdam, pp. 223–231.
Mühlhaus, H.B., Sakaguchi, H., Hobbs, B.E., 1998. Evolution of three-dimensional folds for a non-Newtonian plate in a viscous medium. Proceedings of the Royal Society of London A454, 1–23.
Mühlhaus, H.-B., Dufour, F., Moresi, L., Hobbs, B.E., 2002a. A director theory for viscoelastic folding instabilities in multilayered rock. International Journal of Solids and Structures 39, 3675–3691.
Mühlhaus, H.-B., Moresi, L., Hobbs, B.E., Dufour, F., 2002b. Large amplitude folding in finely layered viscoelastic rock structures. Pure and Applied Geophysics 159, 2311–2333.
Passchier, C.W., Mancktelow, N.S., Grasemann, B., 2005. Flow perturbations: a tool to study and characterize heterogeneous deformation. Journal of Structural Geology 27, 1011–1026.
Price, N.J., 1975. Rates of deformation. Journal of the Geological Society of London 131, 553–575.
Price, N.J., Cosgrove, J.W., 1990. Analysis of Geological Structures. Cambridge University Press, Cambridge.
Ramberg, H., 1961. Relationship between concentric longitudinal strain and concentric shearing strain during folding of homogeneous sheets of rock. American Journal of Science 259, 382–390.
Ramberg, H., 1963. Fluid dynamics of viscous buckling applicable to folding of layered rocks. Bulletin of American Association of Petroleum Geologists 47, 484–505.
Ramberg, H., 1964. Selective buckling of composite layers with contrasted rheological properties, a theory for simultaneous formation of several orders of folds. Tectonophysics 1, 307–341.
Schmalholz, S.M., Podladchikov, Y.Y., 1999. Buckling versus folding: importance of viscoelasticity. Geophysical Research Letters 26, 2641–2644.
Schmalholz, S.M., Podladchikov, Y.Y., 2000. Finite amplitude folding: transition from exponential to layer length controlled growth. Earth and Planetary Science Letters 179, 363–377.
Schmalholz, S.M., Podladchikov, Y.Y., 2001a. Strain and competence contrast estimation from fold shape. Tectophysics 340, 195–213.
Schmalholz, S.M., Podladchikov, Y.Y., 2001b. A spectral/finite difference method for simulating large deformation of heterogeneous, visco-elastic materials. Geophysical Journal International 145, 199–208.
Schmalholz, S.M., Podladchikov, Y.Y., 2001c. Viscoelastic folding: Maxwell versus Kelvin rheology. Geophysical Research Letters 28, 1835–1838.
Sherwin, J.A., Chapple, W.M., 1968. Wavelengths of single layer folds: a comparison between theory and observation. American Journal of Science 266, 167–179.
Smith, R.B., 1975. A unified theory of the onset of single folding, boudinage, and mullion structure. Bulleting of the Geological Society of America 86, 1601–1609.
Smith, R.B., 1977. Formation of folds, boudinage and mullions in non-Newtonian materials. Bulleting of the Geological Society of America 88, 312–320.
Smith, R.B., 1979. The folding of a strongly non-Newtonian layer. American Journal of Science 279, 272–287.
Smoluchowski, M.S., 1909. Über ein gewisses Stabilitätsproblem der Elastizitätslehre und dessen Beziehung zur Entstehung von Faltengebirgen. Akad. Wissensch. Krakau, Math. Kl., 3–20.
Treagus, S.H., 1973. Buckling stability of a viscous single-layer system oblique to the principal compression. Tectonophysics 19, 271–289.
Treagus, S.H., 1981. A theory of stress and strain variations in viscous layers, and its geological implications. Tectonophysics 72, 75–103.
Treagus, S.H., 1983. A new theory of finite strain variation through contrast layers, and its bearing on cleavage refraction. Journal of Structural Geology 5, 351–358.
Treagus, S.H., Sokoutis, D., 1992. Laboratory modeling of strain variation across rheological boundaries. Journal of Structural Geology 14, 405–424.
Treagus, S.H., 1999. Are ratios of rocks measurable from cleavage refraction? Journal of Structural Geology 21, 895–901.
Treagus, S.H., 2003. Viscous anisotropy of two-phase composites, and applications to rocks and structures. Tectonophysics 372, 121–133.
Treagus, S.H., Fletcher, R.C., 2009. Controls of folding on different scales in multilayered rocks. Journal of Structural Geology 31, 1340–1349.
Whiting, A.I.M., Hunt, G.W., 1997. Evolution of nonperiodic forms in geological folds. Mathematical Geology 29, 705–723.
Williams, J.R., Lewis, R.W., Zienkiewicz, O.C., 1977. A finite-element analysis of the role of initial pertabations in the folding of a single viscous layer. Tectonophysics 45, 187–200.
Zhang, Y., Hobbs, B.E., Ord, A., Mühlhaus, H.B., 1996. Computer simulation of single-layer buckling. Journal of Structural Geology 18, 643–655.
Zhang, Y., Mancktelow, N.S., Hobbs, B.E., Ord, A., Mühlhaus, H.B., 2000. Numerical modelling of single-layer folding: clarification of an issue regarding the possible effect of computer codes and the influence of initial irregularities. Journal of Structural Geology 22, 1511–1522.